

Imaging the destruction of a rotating regular black hole

M. F. Fauzi¹, H. S. Ramadhan¹, A. Sulaksono¹, Hasanuddin²

¹Departemen Fisika, FMIPA, Universitas Indonesia, Depok 16424, Indonesia

²Program Studi Fisika, FMIPA, Universitas Tanjungpura, Pontianak 78124, Indonesia

E-mail: hramad@sci.ui.ac.id

Abstract. A regular black hole, unconstrained by the weak cosmic censorship conjecture, can exceed its critical spin limit and transition into a superspinar. In this paper, we investigate the observational appearance of a rotating regular black hole, specifically the Ghosh black hole and its superspinar counterpart, when surrounded by a thin accretion disk. The resulting images reveal distinct features: the black hole closely resembles its Kerr counterpart with slight deviations, while the superspinar configuration exhibits an inner photon ring structure. Furthermore, we explore the image transition of the Ghosh black hole that has been recently destroyed by the capture of a test particle. The results show that the inner photon ring undergoes gradual transitions over time, which depend on the additional angular momentum gained by the black hole. Our findings also suggest that the transition timescale becomes relevant for supermassive black holes with masses approximately twice that of M87*, making these effects potentially observable with future high-resolution instruments.

Keywords: rotating regular black hole, superspinar, appearance

1. Introduction

Black holes (BHs), as predicted by general relativity (GR), offer profound insights into the nature of spacetime and gravity. Observationally, the study of BHs has entered a groundbreaking era with the advent of the Event Horizon Telescope (EHT). The EHT has successfully captured images of supermassive BHs such as M87* [1,2] and Sgr A* [3]. These images reveal a central shadow surrounded by a bright, donut-shaped emission structure, consistent with the presence of an event horizon and an encircling accretion disk. To further test GR, numerous studies have simulated BH shadows and images [4–12], exploring potential deviations from the Kerr (or Kerr-Newman) solutions and providing valuable predictions for future observations.

Theoretically, however, BHs still present fundamental challenges. Their solutions generically exhibit two singular features: the event horizon(s), associated with infinite time dilation, and the spacetime singularity, where curvature diverges. Both static and

rotating BH solutions are generically afflicted by these singularities. In the case of charged BHs, the existence of horizons is constrained by the *weak cosmic-censorship conjecture* (WCCC), which asserts that singularities must remain hidden behind an event horizon [13]. For instance, the Kerr-Newman solution is subject to the condition $M^2 > a^2 + Q^2$, where M , a , and Q represent the BH's mass, angular momentum (spin), and electric charge, respectively. If this bound is violated, the horizon disappears, exposing a *naked singularity*, a scenario that challenges the very foundation of classical GR.

One approach to addressing the singularity problem is the introduction of *regular black holes* (RBHs), which have primarily been studied in static cases. The first non-singular BH solution was proposed by Bardeen [14], who introduced a new parameter in the metric to regulate the singularity by replacing it with a regular de Sitter core. Later, Ayon-Beato and García demonstrated that the Bardeen metric could be interpreted as a charged BH sourced by *non-linear electrodynamics* (NLED) [15]. Various mechanisms have since been proposed to construct RBH solutions, including NLED [15–19], de Sitter vacuum modifications [20, 21], and quantum gravity effects [22–24]. A distinctive feature of RBHs is that they are not constrained by the WCCC, allowing for horizonless configurations. Once a static regular metric is obtained, its rotating counterpart can be derived using the Newman-Janis algorithm [25].

A class of static NLED-based RBH solutions has been proposed in various studies by modifying the Schwarzschild metric through an exponential-type probability distribution [26–29]. Using the Newman-Janis transformation, Ghosh later derived its rotating counterpart [30]. This rotating solution exhibits significant deviations from the classical Kerr-Newman solution, particularly in its horizon structure, ergoregion, and photon sphere. For instance, the photon ring structure differs significantly from that of Kerr BHs, highlighting distinct characteristics in the photon sphere's properties [31]. Further analysis of the ergosphere and shadow reveals that their sizes and shapes are highly sensitive to parameters such as charge and spin, resulting in a richer structure compared to the Kerr solution [32]. Additionally, studies of spherical orbits (both photon and timelike) indicate that the corresponding trajectories exhibit larger latitudinal oscillation amplitudes as the Ghosh parameter increases, underscoring the influence of this parameter on orbital dynamics [33].

Another particularly intriguing study was done by Eichhorn and Held [34], where they examined RBHs within the framework of asymptotic safety gravity [24, 35]. Their findings suggest that *overspinning*, a scenario in which a BH's angular momentum exceeds its critical value (leading to the destruction of the event horizon), could have profound observational consequences. Specifically, the resulting image exhibits additional ring-like secondary images within the primary shadow, effectively lighting up the BH and increasing the overall observed intensity. This brightening occurs instantaneously, as the horizon is globally resolved in the modified spacetime. Furthermore, instead of a gradual transition, the intensity undergoes a sudden, discontinuous shift once the angular momentum surpasses the critical threshold.

In this study, we adopt the definition of *superspinar* as proposed in Ref. [36]: rotating BH spacetime with angular momentum exceeding a critical threshold, $a^2 > a_c^2$. In the classical Kerr solution, such a configuration corresponds to a naked singularity, which may be rendered physically viable through string-theoretic effects [37–39]. In the case of rotating RBH, the superspinar solution might imply something entirely different, depending on the theory used to construct the metric. In both cases, the superspinar could potentially be obtained by *destroying* the BH, *i.e.*, resolving the horizon by sending a test particle with specific angular momentum to be captured by the extremal or near-extremal BH [40–43]. While this mechanism is intriguing, we shall not delve further into its details. Instead, in this work we focus on analyzing the appearance of Ghosh BHs and their superspinar counterparts when surrounded by a thin accretion disk. Inspired by the lighting-up scenario [34], we take a different approach to image transition; we simulate the image transition over a time interval following the recent destruction of an RBH by a test particle with a certain angular momentum. Furthermore, we investigate whether the image intensity transition time is relevant to our observations.

This paper is organized as follows. In Sec. 2, we provide a brief overview of the rotating RBH model employed in our study. In Sec. 3, we introduce the Hamiltonian formalism used for numerically computing null geodesics, which serves as the foundation for our ray-tracing procedure to generate BH images. In Sec. 4, we briefly discuss the accretion disk model, and proceed to the image results and analysis. Sec. 5 is devoted to examining the image transition scenario, presenting the corresponding simulated images, and assessing their observational implications. Finally, in Sec. 6, we summarize our findings and provide concluding remarks.

2. Regular rotating black hole and superspinar

A general form of a rotating BH metric in Boyer-Lindquist coordinates is given by

$$\begin{aligned}
 ds^2 = & - \left(1 - \frac{2m(r)r}{\Sigma} \right) dt^2 - \frac{4am(r)r}{\Sigma} \sin^2 \theta dt d\phi \\
 & + \Sigma \left(\frac{dr^2}{\Xi} + d\theta^2 \right) + \frac{\mathcal{A}}{\Sigma} \sin^2 \theta d\phi^2,
 \end{aligned} \tag{1}$$

with

$$\begin{aligned}
 \Sigma & \equiv r^2 + a^2 \cos^2 \theta, \\
 \Xi & \equiv r^2 + a^2 - 2m(r)r, \\
 \mathcal{A} & \equiv (r^2 + a^2)^2 - \Xi a^2 \sin^2 \theta,
 \end{aligned} \tag{2}$$

and a is the spin parameter. Ghosh constructed a rotating RBH by adopting a mass function of the form [29, 30]

$$m(r) = Me^{-k/r}, \tag{3}$$

where M is the mass and k is the new parameter introduced to regularize the metric. Notably, all curvature invariants remain finite everywhere. In particular, the Kretschmann scalar,

$$K \equiv R^{\alpha\beta\gamma\kappa}R_{\alpha\beta\gamma\kappa} \rightarrow 0, \quad (4)$$

as $r \rightarrow 0$, ensuring the absence of a central singularity.

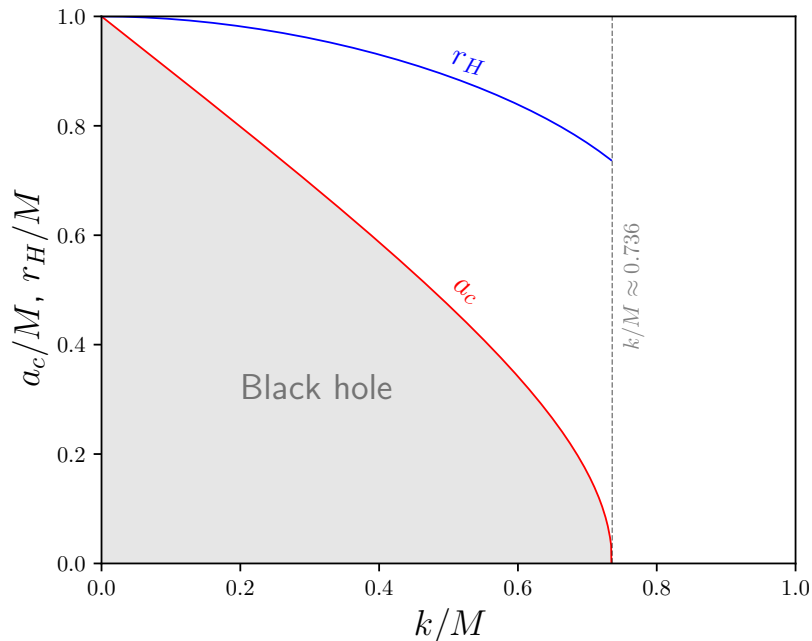


Figure 1. Extremal value of a/M value (red line) and its corresponding horizon radius r_H/M (blue line) as functions of k/M . The grey shaded area depicts the BH configuration where the spacetime contains horizon(s), while the region outside (with $a > 0$) corresponds to the superspinar configuration.

The event horizon radii r_{\pm} are determined by the condition $\Xi = 0$, which leads to the equation

$$r_{\pm} + a^2 - 2Me^{-k/r_{\pm}} = 0. \quad (5)$$

These roots can be obtained numerically. In general, similar to its singular counterpart, an RBH can exhibit three possible configurations: horizonful, extremal, and horizonless. The extremal condition is obtained by simultaneously solving

$$\Xi = \partial_r \Xi = 0. \quad (6)$$

For the Ghosh mass function, there exists a lower bound on the parameter k required to support a horizonful configuration. In the non-rotating limit ($a = 0$), this threshold is found to be approximately $k \approx 0.736M$. The extremal values of the configuration in the parameter space of k and a are illustrated in Fig. 1.

It is useful to define the *lapse function*, α . For an axially symmetric spacetime, it is defined as

$$\alpha^2 = -g_{tt} + \frac{g_{t\phi}^2}{g_{\phi\phi}}. \quad (7)$$

As the name suggests, this quantity measures the proper time lapse of a particle within the given spacetime. In spherically symmetric spacetime, it reduces to the well-known $\alpha^2 = -g_{tt}$, associated with time dilation. Figure 2 shows the lapse function for Ghosh spacetime for several values of k/M and a/M . The point where the lapse function reaches zero aligns with the horizon location ($\Xi = 0$), indicating that the horizon is indeed associated with infinite time. It can also be seen that increasing either a and k leads to a higher minimum of the lapse function. Consequently, the time dilation effect is stronger for lower values of both parameters.

3. Geodesics around axially symmetric spacetime

The dynamics of photon around this RBH is determined by solving the corresponding null geodesic equations. Here, we adopt the Hamiltonian formalism to derive the equations of motion (EoM) and numerically integrate them, following the approach outlined in Refs. [44, 45]. Below, we provide a concise overview of the formalism and its implementation for our specific case.

In general, the rotating metric can be expressed in the form

$$g_{\mu\nu} = \begin{pmatrix} -\alpha^2 + \beta_k \beta^k & \beta_i \\ \beta_j & \gamma_{ij} \end{pmatrix}, \quad (8)$$

where β_j is the shift three vector, and γ_{ij} represents the spatial components of $g_{\mu\nu}$. Greek and Latin indices label the spacetime and spatial coordinates, respectively. The inverse metric take the form

$$g^{\mu\nu} = \begin{pmatrix} -1/\alpha^2 & \beta^i/\alpha^2 \\ \beta^j/\alpha^2 & \gamma^{ij} - \beta^i \beta^j/\alpha^2 \end{pmatrix}, \quad (9)$$

where γ^{ij} is the inverse of γ_{ij} , and $\beta^j = \gamma^{ij} \beta_i$.

The Hamiltonian for a test particle moving in the metric (8) is given by [46]

$$H = \alpha (\gamma^{jk} u_j u_k + \epsilon)^{1/2} - \beta^j u_j, \quad (10)$$

where $u_j = \gamma_{ij} u^i$ is the velocity components of the particle and $\epsilon = 0$ or 1 for null or

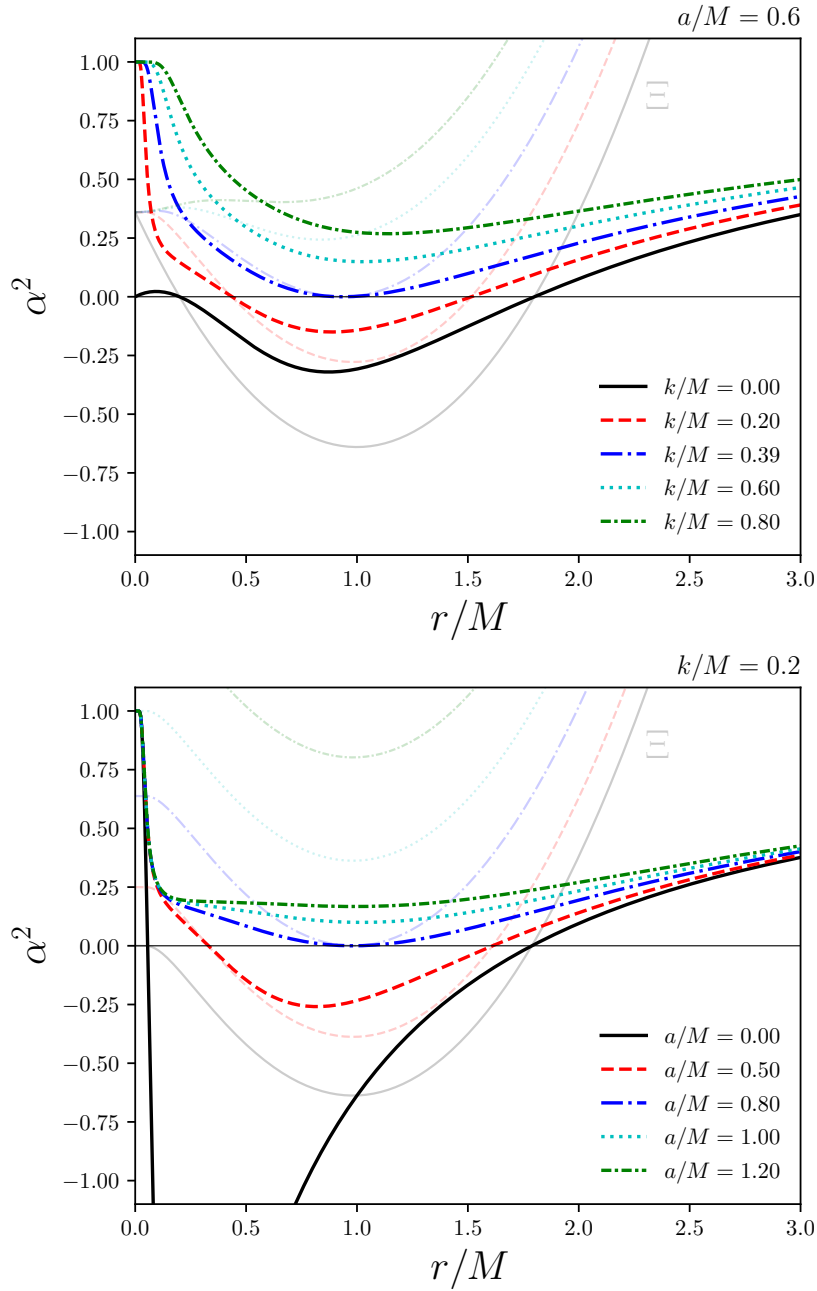


Figure 2. The lapse function α^2 (opaque lines) on the equatorial plane ($\theta = \pi/2$) with constant $a/M = 0.6$ (top) and constant $k/M = 0.2$ (bottom) for several values of k/M and a/M , respectively, and its corresponding Ξ (faint lines). The dash-dotted blue lines represent the extremal configuration with $a = a_c$ for the given k .

massive test particle, respectively. The EoM follow from Hamilton's equations:

$$\begin{aligned} \frac{dx^i}{dt} &= \frac{\partial H}{\partial u_i} \\ &= \frac{\alpha \gamma^{ij} u_j}{(\gamma^{jk} u_j u_k + \epsilon)^{1/2}} - \beta^i, \end{aligned} \quad (11)$$

$$\begin{aligned} \frac{du_i}{dt} &= - \frac{\partial H}{\partial x^i} \\ &= - (\gamma^{jk} u_j u_k + \epsilon)^{1/2} \partial_i \alpha \\ &\quad - \frac{1}{2} \frac{\alpha u_j u_k}{(\gamma^{jk} u_j u_k + \epsilon)^{1/2}} \partial_i \gamma^{jk} + u_j \partial_i \beta^j, \end{aligned} \quad (12)$$

where

$$\begin{aligned} \gamma^{jk} u_j u_k &= \frac{u_r^2}{g_{rr}} + \frac{u_\theta^2}{g_{\theta\theta}} + \frac{u_\phi^2}{g_{\phi\phi}}, \\ \beta^j u_j &= \frac{g_{t\phi}}{g_{\phi\phi}} u_\phi. \end{aligned} \quad (13)$$

Eqs. (11)-(12) govern the geodesic motion of particles and light rays.

One key advantage of this Hamiltonian formalism is its ability to directly compute the trajectory in terms of coordinate time. This feature is particularly useful for analyzing travel time effects on image transitions, which will be discussed in Sec. 5. Instead of solving four coupled second-order ordinary differential equations, often rewritten as eight coupled first-order equations in numerical computations, this approach reduces the system to just six first-order equations for the spatial components, while the time component is implicitly accounted for through the integration step size.

In the superspinar case, a particle may eventually reach the core at $r = 0$. However, the geodesic equations in Boyer-Lindquist coordinates can yield solutions that extend into the unphysical region $r < 0$. Since this region has no physical meaning in our model, we simply disregard it. In the figures presented below, this region is shaded in gray. According to Ref. [34], this region is proposed to be where quantum gravity effects become significant. In such a scenario, modifications to the geodesic equations arising from quantum gravity are expected to prevent particles from reaching this region.

4. Optical appearance involving thin accretion disk

4.1. Thin accretion disk

Simulating BH images generally requires a ray-tracing procedure, which involves computing photon trajectories or null geodesics. In this study, we assume an optically and geometrically thin accretion disk with monochromatic emission. An optically thin accretion disk is transparent, allowing light to pass through without significant absorption or scattering, a characteristic often associated with supermassive BHs [47]. The geometrically thin assumption confines the disk to an infinitesimally narrow region

in the equatorial plane ($\theta = \pi/2$), significantly simplifying the detection algorithm. Furthermore, we incorporate the effects of accretion flow and gravitational redshift, which will be discussed in detail later.

4.1.1. Intensity profile The accumulation of matter in an accretion disk typically results in electromagnetic emission. For simplicity, we consider an emission profile $I_e(r)$, which depends on the matter density and temperature of the disk. We adopt the Gralla-Lupsasca-Marrone (GLM) model [48], given by

$$I_e(r) = \frac{\exp\left\{-\frac{1}{2}\left[\gamma + \operatorname{arcsinh}\left(\frac{r-\mu}{\sigma}\right)\right]^2\right\}}{\sqrt{(r-\mu)^2 + \sigma^2}}, \quad (14)$$

where γ , μ , and σ are parameters that determine the shape of the emission profile. Compared to exponential cut-off models (see, e.g., Refs. [49–51]), the GLM profile offers a continuous intensity function with tunable smoothness, controlled by the parameters σ and γ . This model was found to closely match the observational predictions for the intensity profiles of astrophysical accretion disks, as obtained through general relativistic magnetohydrodynamics simulations [52], and has been used in several other investigations of BHs and ultracompact objects' appearance. [53–58]. We set these parameters as $\gamma = -2$, $\mu = R_{ISCO}$, and $\sigma = M/4$, where R_{ISCO} denotes the radius of the *innermost stable circular orbit* (ISCO) for a massive particle. This model assumes that emission peaks near the ISCO radius and ceases beyond it, as any massive particle crossing within the ISCO inevitably spirals toward the BH, leading to a peak in matter density around this radius.

4.1.2. Accretion flow and innermost stable circular orbit We assume the accretion flow to be Keplerian on the equatorial plane, described by the (timelike) 4-velocity u_e^ν

$$u_e^\nu = (u_e^t, u_e^r, 0, u_e^\phi). \quad (15)$$

Additionally, we assume that the matter in the disk does not experience any radial drift, implying $u_e^r = 0$. The azimuthal component u_e^ϕ is given by [59, 60]

$$u_e^\phi = \frac{\Omega}{\sqrt{-g_{tt} - (2g_{t\phi} + g_{\phi\phi}\Omega)\Omega}}, \quad (16)$$

$$\Omega = \frac{-g_{t\phi,r} \pm \sqrt{g_{t\phi,r}^2 - g_{tt,r}g_{\phi\phi,r}}}{g_{\phi\phi,r}}, \quad (17)$$

where the \pm sign corresponds to the direction of the accretion flow orbit: prograde or retrograde. Imposing the 4-velocity condition,

$$g_{tt}(u_e^t)^2 + g_{\phi\phi}(u_e^\phi)^2 + 2g_{t\phi}u_e^t u_e^\phi = -1, \quad (18)$$

we obtain the time component u^t as

$$u_e^t = \frac{g_{t\phi}u_e^\phi \pm \sqrt{-g_{tt} + (g_{t\phi}^2 - g_{tt}g_{\phi\phi})(u_e^\phi)^2}}{-g_{tt}}, \quad (19)$$

where we select only the positive root.

The 4-velocity components of the accretion flow determine the redshift effects, denoted by the factor g , which include both the gravitational redshift and the relativistic Doppler effect. A source emitting light at frequency ν_e will experience a redshift as it propagates toward the observer, resulting in an observed frequency ν_o . Their relationship is given by [59–61]

$$\nu_o = g\nu_e, \quad g = \frac{-k_\mu u_o^\mu}{-k_\nu u_e^\nu}, \quad (20)$$

where the subscript e and o refer to the emitting frame (accretion disk) and observer frame, respectively, and $k_\mu = k^\nu g_{\mu\nu}$ is the photon 4-momentum (null vector). Since we assume a static, distant observer, the observer's 4-velocity is given by $u_o^\mu = (1, 0, 0, 0)$. Using the 4-velocity of the accretion flow, the redshift factor simplifies to

$$g = \left(u_e^t + \frac{k_\phi}{k_t} u_e^\phi \right)^{-1}. \quad (21)$$

The observed intensity is determined using the Lorentz-invariant relation $I_e^\nu/\nu_e^3 = I_o^\nu/\nu_o^3$. Integrating over all frequencies gives the total observed intensity

$$I_o(r) = \int I_o^\nu(r) d\nu_o = g^4 I_e(r). \quad (22)$$

The accretion flow features an ISCO, whose radius is determined by solving for a point where $u^r = \partial_r V_t(r) = \partial_{rr} V_t(r) = 0$, where $V_t(r)$ represents the effective potential for timelike geodesics [62],

$$V_t(r) = -\frac{1}{2r^2} (g_{tt}L^2 + g_{t\phi}EL + g_{\phi\phi}E^2) + \frac{1}{2} \quad (23)$$

The L and E are integration constants, and for circular orbits, they can be determined by

$$\begin{aligned} L &= \frac{g_{\phi\phi}\Omega + g_{t\phi}}{\sqrt{-g_{\phi\phi}\Omega^2 - 2g_{t\phi}\Omega - g_{tt}}}, \\ E &= -\frac{g_{t\phi}\Omega + g_{tt}}{\sqrt{-g_{\phi\phi}\Omega^2 - 2g_{t\phi}\Omega - g_{tt}}}. \end{aligned} \quad (24)$$

For stable circular orbits, we require

$$g_{tt,rr}L^2 + 2g_{t\phi,rr}LE + g_{\phi\phi,rr}E^2 - 2 \Big|_{r=R_{ISCO}} \leq 0 \quad (25)$$

and this quantity is zero at the ISCO. Hence, substituting Eq. (24) into Eq. (25) and solve for r , we will eventually obtain the R_{ISCO} .

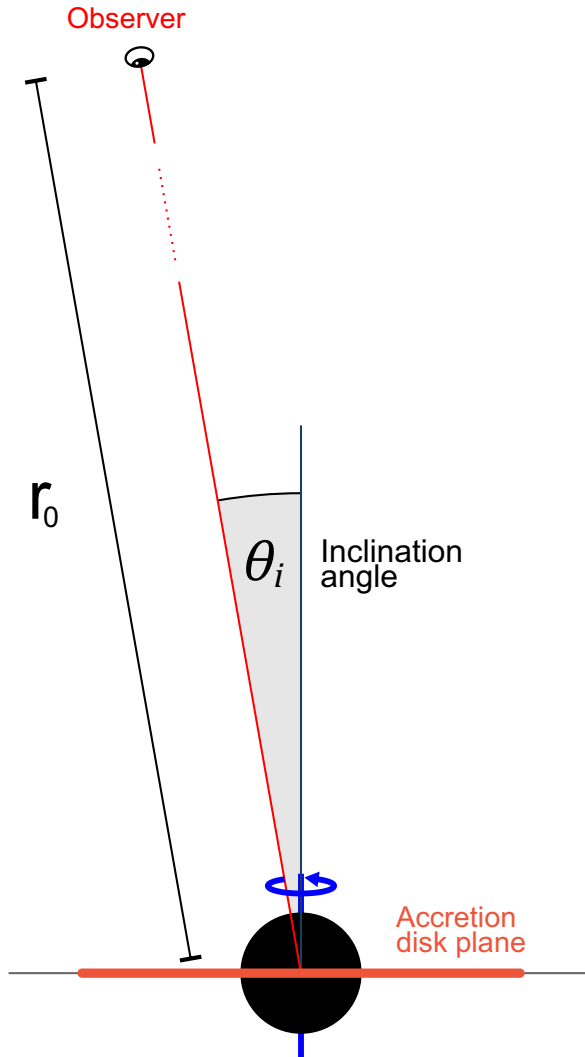


Figure 3. A 2D illustration of the ray tracing mechanism. Light rays are emitted from the observer’s position with a distance of r_0 from the object, and directed towards the central point, $r = 0$. The accretion disk, represented by the orange thick line, lies in the equatorial plane ($\theta = \pi/2$) and follows a retrograde orbit relative to the object’s spin.

4.2. Ray tracing and image results

To generate simulated images of curved spacetime, we employ a ray-tracing procedure that involves computing null geodesics using the Hamiltonian formalism discussed in Sec. 3, utilizing the backward-integration method. Specifically, we adopt the pinhole ray-tracing technique, where light rays are traced backward from an observer positioned at near-infinity, for instance, at $r_0 = 500M$. Each time a ray intersects the accretion disk on the equatorial plane, the corresponding intensity at that point—accounting for redshift effects—is recorded and mapped to the appropriate pixel on the observer’s screen. The ray-tracing scheme is illustrated in Fig. 3.

We generate images of both BH and superspinar configurations by varying the

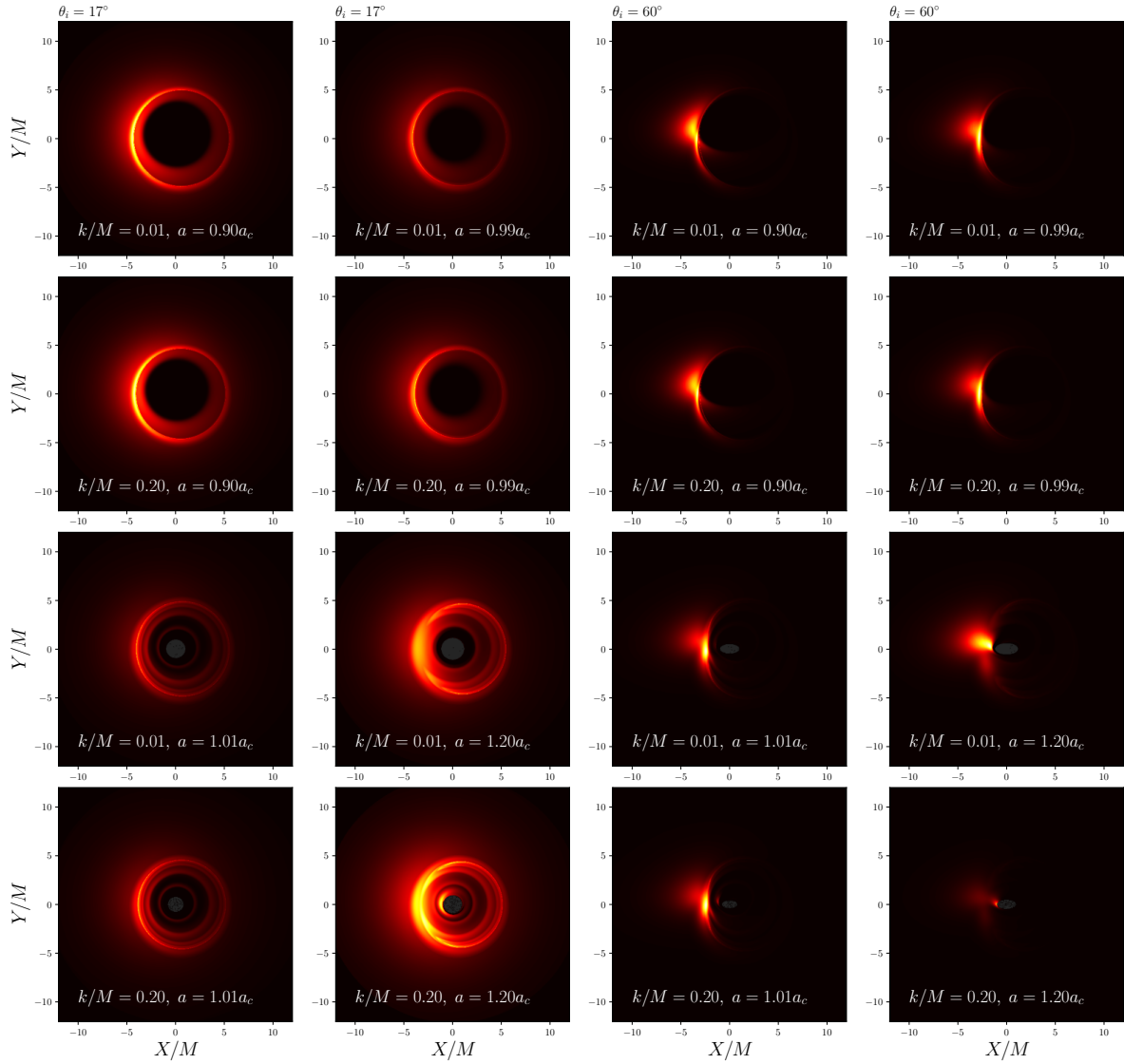


Figure 4. Appearance of the Ghosh RBH (first and second rows) and its superspinar counterparts (third and fourth rows) surrounded by a thin accretion disk for inclination angles $\theta_i = 17^\circ$ (first and second columns) and $\theta_i = 60^\circ$ (third and fourth columns). The images are normalized by their maximum intensity. The greyed region on the superspinar images represents the area where $r < 0$.

parameter k , as shown in Fig. 4. Specifically, we choose $k/M = \{0.01, 0.20\}$ with $a/a_c = \{0.90, 0.99, 1.01, 1.20\}$, so that one can investigate the effect of the free parameter at its minimum value and at a slightly higher value, as well as the effect of spin near the extremal configuration and beyond. The ISCO value for both configurations are presented in Table 1. In the BH case, the image features generally resemble those of a typical rotating BH spacetime. At low inclination angles, the image consists of an almost perfectly circular dark patch, surrounded by a ring-shaped intensity accumulation, which corresponds to the secondary image. At higher angles, the dark patch becomes more distorted, forming a deformed circular shadow encircled by a thin ring. This thin ring is

Figure	Spacetime	a/a_c	k/M	r_{ISCO}/M
Fig. 4	Ghosh	0.90	0.01	2.32
		0.99		1.45
		1.01		0.75
		1.20		0.69
		0.90	0.20	2.20
		0.99		1.41
		1.01		0.65
		1.20		0.19
Figure	Spacetime	a/M	k/M	r_{ISCO}/M
Fig. 5	Ghosh	0.50M	0.10	3.85
			0.20	3.42
		0.70M	0.10	2.92
			0.20	2.33
	Kerr	0.50M	-	4.23
		0.70M	-	3.39

Table 1. The value of ISCO for each configuration we tested.

also present at low angles but overlaps with the accumulated intensity of the secondary image. As the inclination increases, the thin ring slightly separates from the dark region, and becomes the boundary of the deformed dark patch.

In contrast, the superspinar configuration exhibits distinctly different image features. At low inclination angles with $a = 1.01a_c$, multiple visible ring-like secondary images appear, whereas for $a = 1.20a_c$, a crescent-shaped secondary image is formed. At higher inclination angles, these rings become dimmer and less prominent. We also observe that the free parameter k does not significantly affect the appearance in the superspinar configuration with slightly higher spin above the critical limit. However, as the spin increases, the appearance changes dramatically. A larger value of k leads to a bright peak intensity near the center of the image. This is primarily due to the much lower ISCO value for $k/M = 0.20$ compared to $k/M = 0.01$, which, according to our accretion disk model, causes the peak intensity to shift closer to the center.

These superspinar images differ significantly from those presented in other studies, such as Refs. [4] and [34]. This discrepancy mainly stems from the different intensity profiles used for the accretion disk and the location at which the emission ceases. In our approach, the disk emission profile stops slightly below ISCO, determined via Eq.(25). On the other hand, Ref. [34] impose a relatively sharp cutoff at $4M$ and $5M$, respectively. This choice significantly affects the appearance of secondary images, making the ring-like features more prominent in their results compared to ours. Our approach accounts for redshift effects, which appear to be absent in Refs. [34]. Notably, the inclusion of Doppler redshift introduces asymmetry in the observed intensity, making one side of the image appear brighter than the other. This asymmetry serves as a distinguishing

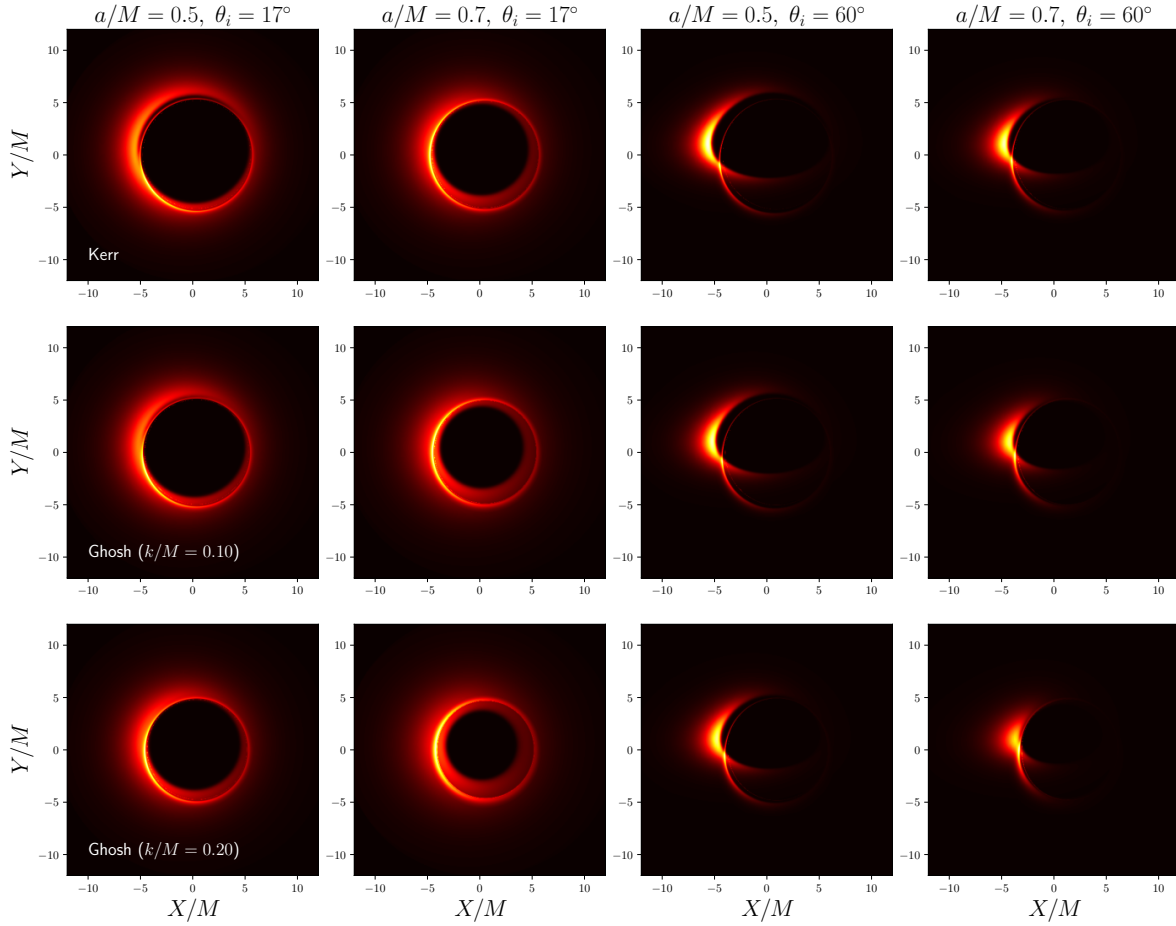


Figure 5. Image comparison between the Kerr (first row) and the Ghosh (second and third rows) BHs with the same spin parameter, for inclination angles $\theta_i = 17^\circ$ (first and second column) and $\theta_i = 60^\circ$ (third and fourth column). The intensity of each image is normalized with respect to its maximum intensity.

feature of models that incorporate relativistic redshift effects.

Finally, to compare the image features of the Ghosh BH with its singular counterpart (the Kerr BH) we analyze how the parameter k influences the appearance of a BH surrounded by a thin accretion disk. The resulting images are shown in Fig. 5, while the intensity cross-sections along both the mid x -axis and y -axis are presented in Fig. 6 for a quantitative comparison of their differences.

It is clear that the additional parameter k affects both the sizes of the ISCO and the photon ring radius of the BH. In our case, both decrease as k increases, with the ISCO being more strongly affected. This causes the secondary photon ring image to overlap with the direct emission from the accretion disk at larger k values, as shown in the first column of Fig. 5. For $a/M = 0.5$ and $\theta_i = 17^\circ$, the photon ring in Kerr spacetime is clearly separated in the upper portion of the image. In contrast, for Ghosh spacetime with $k/M = 0.20$, the photon ring overlaps with the inner direct emission from the accretion disk, specifically at the ISCO. Upon examining the intensity cross-section

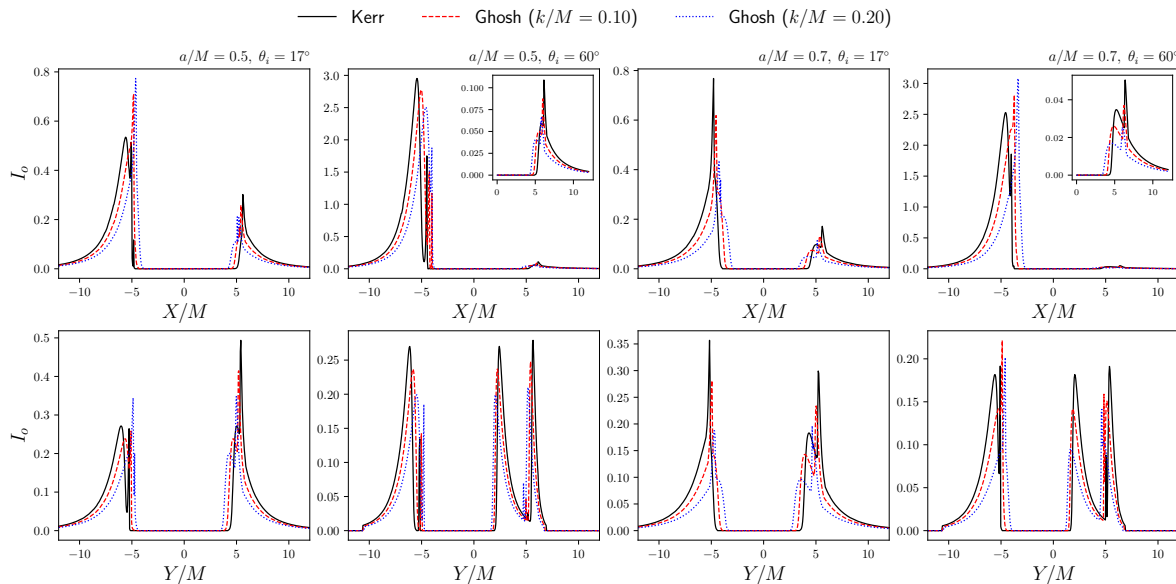


Figure 6. Intensity cross-section corresponding to the central region of the x -axis (top row) and y -axis (bottom row) for each images presented in Fig. 5. The sharp peaks indicate the locations of photon ring emissions.

in Fig. 6, it is evident that the intensity also decreases for smaller ISCO radii. This reduction is primarily attributed to the gravitational redshift effect, which, analogous to the spherically symmetric spacetime, becomes more significant near the horizon, as the redshift factor is given by $g = \sqrt{-g_{tt}}$ with static fluids.

5. Imaging the black hole's destruction

Consider an extremal rotating RBH ($a = a_c$) surrounded by a thin accretion disk. Suppose that the BH captures a particle, gaining an additional angular momentum δ so that $a = a_c \rightarrow a_c + \delta$, becoming a regular superspinar. This transition destroys the event horizons, allowing light to pass through the core of the BH.

In Ref. [34], it is shown that overspinning a RBH leads to an instantaneous *lighting-up* effect, when the secondary image on the central region appears instantaneously as the BH transitions to a superspinar. This occurs because the event horizon is resolved globally, allowing light to pass through the central region as soon as the spin parameter exceeds the critical value a_c , even for an arbitrarily small increase δ . However, if one takes into account the time delay effect, a delayed lighting-up may be observed, resulting in a gradual transformation of the image. It is important to note that in this scenario, the gradual change in the observed image is not due to a continuous variation in the spin parameter a as discussed in [34], but rather due to the progression of time t .

The time elapsed by the observer as a light travels from τ_0 to τ_f is given by [45, 63]

$$\Delta t = \int_{\tau_0}^{\tau_f} k^t d\tau = \int_{\tau_0}^{\tau_f} \sqrt{\frac{\gamma^{ij} k_i k_j}{\alpha^2}} d\tau, \quad (26)$$

where k^i represents the null 4-velocity, and τ is an affine parameter. It can be seen that the time delay is most significant at the minimum value of α on the equatorial plane (see Fig. 2). If light emitted from the accretion disk undergoes multiple orbits near this minimum region before escaping to infinity, the travel time observed by a distant observer will be significantly longer. This results in the delay of the formation of the secondary images. Based on this simple reasoning, we expect it is possible to observe a delayed lighting-up of a the transition from a rotating RBH to a superspinar.

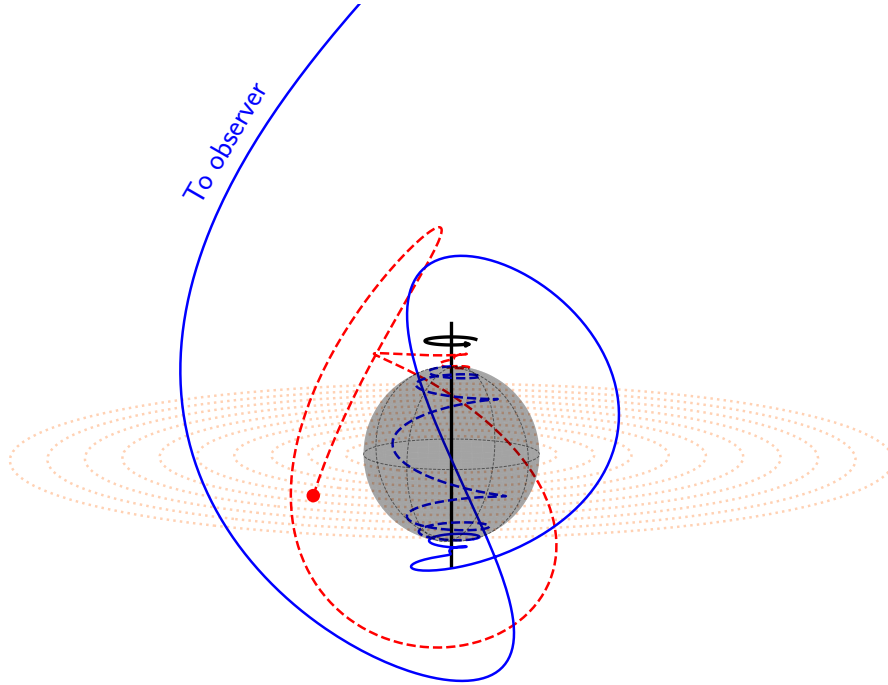


Figure 7. The photon trajectory and its recorded travel time mechanism, depicting their journey to the observer. A photon is emitted from the accretion disk, originating from the red solid circle, and travels through the “imaginary” horizon (represented by the greyed spherical region) before reaching the observer. Our algorithm records only the travel time associated with the blue lines: the dashed line represents the photon’s trajectory inside the imaginary horizon (interior of the superspinar), while the solid line indicates its path after exiting this region.

5.1. Image and intensity transition

Since a BH and a superspinar have different spacetime structure, the ray-tracing procedure must be slightly modified to generate the transition images. Several assumptions are employed to simplify the calculation. First, we neglect any dynamical effects inside the spacetime, even though the BH’s destruction could, in principle, induce dynamical changes. Instead, for each tested configuration, we assume the final state of the object (a superspinar with $a = a_c + \delta$) and impose a *stopping condition* at the at the extremal horizon radius for the initial image at $t = 0$, despite the absence of an actual

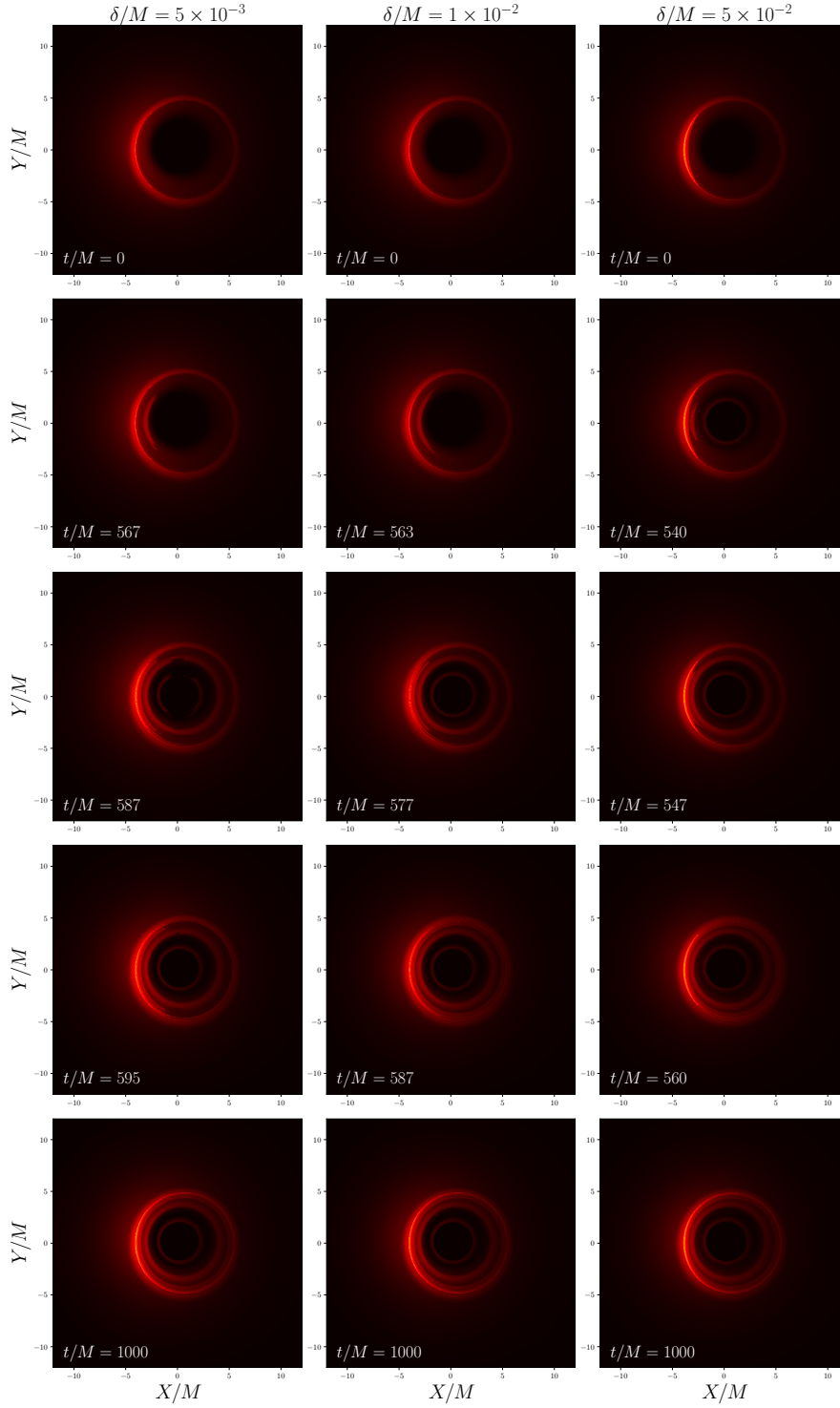


Figure 8. The evolution of the recently destroyed extremal Ghosh BH ($a = a_c$) over time into its superspinar counterparts ($a = a_c + \delta$) with an inclination angle of $\theta_i = 17^\circ$ for $\delta/M = 5 \times 10^{-3}$ (first column), $\delta/M = 1 \times 10^{-2}$ (second column), and $\delta/M = 5 \times 10^{-2}$ (third column). The image transition does not start at $t/M = 0$, but rather at a later time as shown in Fig. 9. The inaccessible region (represented by the grey area in Fig. 4) of the superspinar remains present in these images; however, we do not explicitly show them in the current figure.

event horizon. While this approach may seem *over-simplified*, it provides a practical framework for image generation while effectively capturing the formation of secondary images within the previously shadowed region. Fig. 7 illustrates how the travel time of each rays are recorded. The whole blue and red paths represent the actual photon trajectories, obtained by solving the corresponding null geodesic equations, Eqs. (11)-(12).

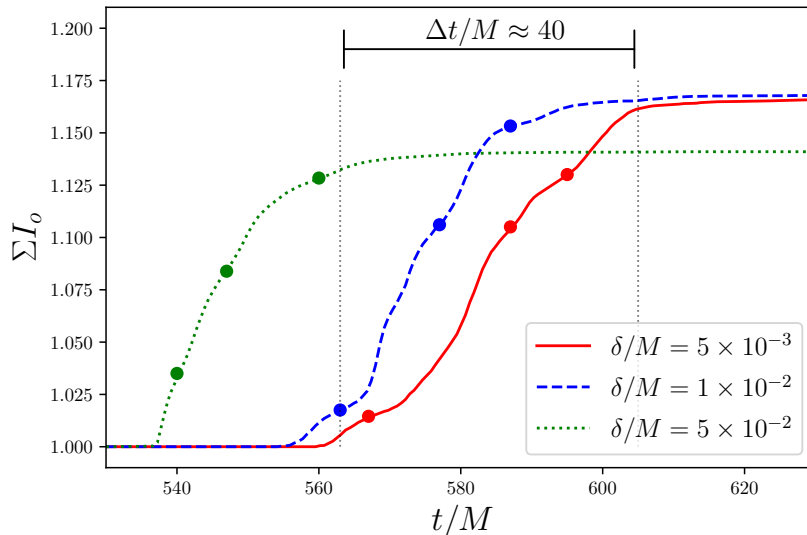


Figure 9. Evolution of the integrated intensity ΣI_o over time, normalized to its initial value at $t/M = 0$. The filled circles indicate the time corresponding to the images in the second to fourth rows of Fig. 8.

Here, we examine the transition by generating the images over a time interval and analyzing the temporal evolution of the integrated intensity ΣI_o in Figs. 8 and 9, respectively. To maximize the spin parameter, we set $\delta/M = \{5 \times 10^{-3}, 1 \times 10^{-2}, 5 \times 10^{-2}\}$ with $k/M = 0.01$, corresponding to $a_c/M \approx 0.9899$. The initial time $t = 0$ marks the moment when the BH captures a particle and transitions into a superspinner with $a = a_c + \delta$. Our investigation reveals that the most distinct differences in appearance and intensity between the BH and superspinner configurations occur low inclination angle, as shown in Fig. 4. Thus, we only consider image transitions at an inclination of $\sim 17^\circ$.

For small increments in angular momentum δ , specifically for $\delta/M = 5 \times 10^{-3}$ and $\delta/M = 1 \times 10^{-2}$, the image transition process follows a similar pattern: the middle secondary ring appears first, followed by the central and outer rings, before settling into the final image state, as shown in the first and second columns of Fig. 8. This transition occurs over approximately $t \approx 40M$ for both cases, with the transition for $\delta/M = 5 \times 10^{-3}$ taking slightly longer (see the red and blue lines in Fig. 9). In contrast, for $\delta/M = 5 \times 10^{-2}$ the transition process is significantly different. The secondary ring images appear sequentially from the center outward to the outer layers, as shown in the third column of Fig. 8. The transition time is also significantly shorter, around $t \approx 30M$, with a steeper initial integrated intensity transition (see the green line in Fig. 9).

The time difference arises due to the increased lapse function within the superspinar interior at higher spin values, as shown in Fig. 2. The minimum value of the lapse function decreases for lower spin parameters. Consequently, as indicated in Eq. (26), a smaller increase in angular momentum results in a longer photon travel time to reach the observer, thereby slowing down image transition. Furthermore, variations in the lapse function also affect the photon trajectory, resulting in a distinct transition process for different spin parameters.

These results suggest that the angular momentum of a particle captured by an extremal RBH can, in principle, be distinguished by analyzing the transition time in intensity, as well as the sequence of image transitions and the emergence pattern of secondary ring images. However, the timescale of this transition may not be observable with current instruments since they requires several days to capture the images. Therefore, we will discuss the relevance of these findings with respect to current observational capabilities in the following discussion.

5.2. Is the finding relevant?

One may ask regarding the transition time of the images: *Is it relevant for observation on earth?* Capturing an image of BH with the EHT requires a significant observational period; for instance, the first EHT image of M87* BH was compiled from data collected over an entire week [1]. If the transition timescale is much shorter than the observational period, the transition may be effectively unobservable and thus irrelevant for practical observations.

Let us consider the longest transition time for an inclination of $\theta = 17^\circ$, which is approximately $\Delta t/M \approx 40$. Converting the natural units back to SI, $M \rightarrow GM/c^2$ and $t \rightarrow ct$, we obtain an estimated transition time of $\Delta t = 40GM/c^3$. For the M87* BH, with a mass of approximately $6.5 \times 10^9 M_\odot$ [1], the corresponding transition time is

$$\Delta t_{M87*} \approx 1.28 \times 10^6 \text{ s} \approx 14.7 \text{ days}, \quad (27)$$

roughly twice than the observation time of the EHT. However, despite the comparable timescale, this does not necessarily imply that the transition is directly measurable. These results suggest that such a transition might be more relevant for even more massive BHs.

We can estimate the BH mass at which these phenomena become relevant based on current observational data. For instance, if we aim to capture three observational images during the transition and assume a transition time of approximately $\Delta t = 40 GM/c^3$, the observation must be conducted within intervals of roughly $\Delta t \approx 13.33 GM/c^3$. Given the observational time frame of EHT (~ 7 days) [1], the corresponding relevant BH mass M_{obs} can be determined, resulting in

$$M_{obs} \approx 9.2 \times 10^9 M_\odot, \quad (28)$$

which is less than twice the mass of M87* and remains well below the theoretical

maximum for a BH mass [64]. However, due to overlapping frames in daily observations, the resulting image transition may not be as distinct as depicted in Fig. 8.

6. Summary

In this paper, we explored the characteristics of a RBH and its superspinar counterpart, specifically focusing on the Ghosh BH, which is surrounded by a thin accretion disk. We generated images using a ray-tracing method, employing the Hamiltonian formalism to compute the null geodesics within our ray-tracing code. We also calculated the ISCO radius to define the inner boundary of the accretion disk and analyzed the effects of gravitational and Doppler redshift on the accretion flow. Our findings indicate that the Ghosh BH closely resembles the Kerr BH. As the parameter k increases, both the Ghosh BH's ISCO and photon ring radius decrease. In contrast with the BH spacetime, the lack of horizons in the superspinar case results in a distinctly different image, marked by the presence of inner secondary images. However, these secondary images become less visible at higher inclination angles due to strong Doppler redshift effects, which significantly diminish their intensity.

We also examined the image transition of a recently destroyed rotating RBH: an extremal rotating RBH that captures a test particle with specific angular momentum, effectively removing its horizons and transforming it into a superspinar. The resulting image transitions suggest that the additional angular momentum acquired by the BH can be distinguished by analyzing the formation of secondary images and the timing and shape of their relative intensity evolution. A more substantial increase in angular momentum results in a shorter and more abrupt transition, primarily due to the reduced time dilation effect, as illustrated in Fig. 2 for BHs with higher spin.

Furthermore, we discussed the significance of transition time in the context of current observational capabilities. For a BH with a mass comparable to M87*, the image transition time is approximately two weeks. This duration poses challenges for clear observation with the EHT, which typically requires about one week to capture an image. Therefore, to make meaningful observations of the transition, at least three consecutive weeks of monitoring would be necessary. Based on this, we estimate that the image transition becomes more relevant for BHs significantly more massive than M87*, roughly twice its mass (around $9.2 \times 10^9 M_\odot$), which is still well below the theoretical maximum BH mass [64].

Finally, we highlight several caveats that could inform future investigations. As noted in Sec. 5, we utilized a simplified ray-tracing approach for calculating the image transition. While this method captures essential features, a fully dynamic spacetime model may yield slightly different results. To our knowledge, however, no time-dependent solutions for the destruction of a BH have been established. Additionally, some studies suggest that certain BHs cannot be destroyed through the capture of test particles [40, 65–67]. This indicates a need for deeper exploration into the feasibility of destroying the relevant RBH, which falls outside the scope of our work. We also

assumed a thin accretion disk model with GLM emission profile along with a detection algorithm tailored to record the disk's intensity. Although the GLM profile is extensively utilized in studies of the appearance of BHs and ultracompact objects, it may not be suitable for the superspinar scenario, as it involves extreme spin conditions and could yield distinct disk dynamics in such systems. Moreover, if we had used a complete radiative transfer mechanism and a thick accretion disk model, the transition might have appeared smoother and potentially showing slightly lower intensity due to absorption and scattering of light within the disk material. Nevertheless, we believe that these limitations do not significantly impact the validity of our main results.

Acknowledgements

We thank Byon Jayawiguna for the enlightening discussions. HSR is funded by Hibah Matching-Fund UI-UNTAN No. PKS-002/UN2.F3.D/PPM.00.02/2024. Hasanuddin is supported by Dana DIPA Universitas Tanjungpura No. SP DIPA-023.17.2.677517/2024.

References

- [1] K. Akiyama *et al.* [Event Horizon Telescope], “First M87 Event Horizon Telescope Results. I. The Shadow of the Supermassive Black Hole,” *Astrophys. J. Lett.* **875**, L1 (2019) [arXiv:1906.11238 [astro-ph.GA]].
- [2] K. Akiyama *et al.* [Event Horizon Telescope], “The persistent shadow of the supermassive black hole of M 87. I. Observations, calibration, imaging, and analysis,” *Astron. Astrophys.* **681**, A79 (2024)
- [3] K. Akiyama *et al.* [Event Horizon Telescope], “First Sagittarius A* Event Horizon Telescope Results. I. The Shadow of the Supermassive Black Hole in the Center of the Milky Way,” *Astrophys. J. Lett.* **930**, no.2, L12 (2022) [arXiv:2311.08680 [astro-ph.HE]].
- [4] F. Lamy, E.ourgoulhon, T. Paumard and F. H. Vincent, “Imaging a non-singular rotating black hole at the center of the Galaxy,” *Class. Quant. Grav.* **35**, no.11, 115009 (2018) [arXiv:1802.01635 [gr-qc]].
- [5] A. Held, R. Gold and A. Eichhorn, “Asymptotic safety casts its shadow,” *JCAP* **06**, 029 (2019) [arXiv:1904.07133 [gr-qc]].
- [6] G. P. Li, H. B. Zheng, K. J. He and Q. Q. Jiang, “The shadow and observational images of the non-singular rotating black holes in loop quantum gravity,” [arXiv:2410.17295 [gr-qc]].
- [7] C. Y. Yang, M. I. Aslam, X. X. Zeng and R. Saleem, “Shadow Images of Ghosh-Kumar Rotating Black Hole Illuminated By Spherical Light Sources and Thin Accretion Disks,” [arXiv:2411.11807 [astro-ph.HE]].
- [8] K. J. He, C. Y. Yang and X. X. Zeng, “Optical appearance of the Konoplya-Zhidenko rotating non-Kerr black hole surrounded by a thin accretion disk,” [arXiv:2501.06778 [astro-ph.HE]].
- [9] C. Bambi, K. Freese, S. Vagnozzi and L. Visinelli, “Testing the rotational nature of the supermassive object M87* from the circularity and size of its first image,” *Phys. Rev. D* **100**, no.4, 044057 (2019) [arXiv:1904.12983 [gr-qc]].
- [10] S. Vagnozzi, R. Roy, Y. D. Tsai, L. Visinelli, M. Afrin, A. Allahyari, P. Bambhaniya, D. Dey, S. G. Ghosh and P. S. Joshi, *et al.* “Horizon-scale tests of gravity theories and fundamental physics from the Event Horizon Telescope image of Sagittarius A,” *Class. Quant. Grav.* **40**, no.16, 165007 (2023) [arXiv:2205.07787 [gr-qc]].
- [11] R. Ghosh, M. Rahman and A. K. Mishra, “Regularized stable Kerr black hole: cosmic censorship, shadow and quasi-normal modes,” *Eur. Phys. J. C* **83**, no.1, 91 (2023) [arXiv:2209.12291 [gr-qc]].

- [12] T. Igata, M. Omamiyuda and Y. Takamori, “Gravitational lensing and accretion disk imaging of a Buchdahl dense core,” [arXiv:2502.11755 [gr-qc]].
- [13] R. Penrose, “Gravitational collapse: The role of general relativity,” *Riv. Nuovo Cim.* **1** (1969), 252-276
- [14] J. Bardeen, “Non-singular general-relativistic gravitational collapse,” in *Proc. Int. Conf. GR5, Tbilisi (1968)*, p. 174.
- [15] E. Ayon-Beato and A. Garcia, “The Bardeen model as a nonlinear magnetic monopole,” *Phys. Lett. B* **493**, 149 (2000) [arXiv:gr-qc/0009077 [gr-qc]].
- [16] E. Ayon-Beato and A. Garcia, “Regular black hole in general relativity coupled to nonlinear electrodynamics,” *Phys. Rev. Lett.* **80**, 5056 (1998) [arXiv:gr-qc/9911046 [gr-qc]].
- [17] K. A. Bronnikov, “Regular magnetic black holes and monopoles from nonlinear electrodynamics,” *Phys. Rev. D* **63**, 044005 (2001) [arXiv:gr-qc/0006014 [gr-qc]].
- [18] A. Burinskii and S. R. Hildebrandt, “New type of regular black holes and particle - like solutions from NED,” *Phys. Rev. D* **65**, 104017 (2002) [arXiv:hep-th/0202066 [hep-th]].
- [19] K. A. Bronnikov and R. K. Walia, “Field sources for Simpson-Visser spacetimes,” *Phys. Rev. D* **105**, 044039 (2022) [arXiv:2112.13198 [gr-qc]].
- [20] S. A. Hayward, “Formation and evaporation of regular black holes,” *Phys. Rev. Lett.* **96**, 031103 (2006) [arXiv:gr-qc/0506126 [gr-qc]].
- [21] M. Cadoni, M. De Laurentis, I. De Martino, R. Della Monica, M. Oi and A. P. Sanna, “Are nonsingular black holes with super-Planckian hair ruled out by S2 star data?,” *Phys. Rev. D* **107**, 044038 (2023) [arXiv:2211.11585 [gr-qc]].
- [22] P. Nicolini, “How strings can explain regular black holes,” [arXiv:2306.01480 [gr-qc]].
- [23] A. Ashtekar, J. Olmedo and P. Singh, “Regular black holes from Loop Quantum Gravity,” [arXiv:2301.01309 [gr-qc]].
- [24] A. Eichhorn and A. Held, “Black holes in asymptotically safe gravity and beyond,” [arXiv:2212.09495 [gr-qc]].
- [25] E. T. Newman and A. I. Janis, “Note on the Kerr spinning particle metric,” *J. Math. Phys.* **6**, 915-917 (1965)
- [26] L. Balart and E. C. Vagenas, “Regular black holes with a nonlinear electrodynamics source,” *Phys. Rev. D* **90** (2014) no.12, 124045 [arXiv:1408.0306 [gr-qc]].
- [27] J. C. S. Neves and A. Saa, “Regular rotating black holes and the weak energy condition,” *Phys. Lett. B* **734** (2014), 44-48 [arXiv:1402.2694 [gr-qc]].
- [28] M. Azreg-Aïnou, “Generating rotating regular black hole solutions without complexification,” *Phys. Rev. D* **90** (2014) no.6, 064041 [arXiv:1405.2569 [gr-qc]].
- [29] H. Culetu, “On a regular charged black hole with a nonlinear electric source,” *Int. J. Theor. Phys.* **54**, no.8, 2855-2863 (2015) [arXiv:1408.3334 [gr-qc]].
- [30] S. G. Ghosh, “A nonsingular rotating black hole,” *Eur. Phys. J. C* **75**, no.11, 532 (2015) [arXiv:1408.5668 [gr-qc]].
- [31] R. Kumar and S. G. Ghosh, “Photon ring structure of rotating regular black holes and no-horizon spacetimes,” *Class. Quant. Grav.* **38** (2021) no.8, 8 [arXiv:2004.07501 [gr-qc]].
- [32] S. G. Ghosh, M. Amir and S. D. Maharaj, “Ergosphere and shadow of a rotating regular black hole,” *Nucl. Phys. B* **957** (2020), 115088 [arXiv:2006.07570 [gr-qc]].
- [33] A. S. Alam, L. C. Andaru, B. N. Jayawiguna and H. S. Ramadhan, “Spherical orbits around Kerr-Newman and Ghosh black holes,” *Gen. Rel. Grav.* **56**, no.7, 79 (2024) [arXiv:2404.17277 [gr-qc]].
- [34] A. Eichhorn and A. Held, “Quantum gravity lights up spinning black holes,” *JCAP* **01**, 032 (2023) [arXiv:2206.11152 [gr-qc]].
- [35] A. Platania, “Black Holes in Asymptotically Safe Gravity,” [arXiv:2302.04272 [gr-qc]].
- [36] R. Torres, “Observational and theoretical aspects of superspinars,” *Gen. Rel. Grav.* **57**, no.2, 50 (2025) [arXiv:2407.14851 [gr-qc]].
- [37] E. G. Gimon and P. Horava, “Astrophysical violations of the Kerr bound as a possible signature

- of string theory,” *Phys. Lett. B* **672** (2009), 299-302 [arXiv:0706.2873 [hep-th]].
- [38] B. Nguyen, P. Christian and C. k. Chan, “Shadow Geometry of Kerr Naked Singularities,” *Astrophys. J.* **954** (2023) no.1, 78 [arXiv:2302.08094 [astro-ph.HE]].
- [39] Z. Stuchlik and J. Schee, “Appearance of Keplerian discs orbiting Kerr superspinars,” *Class. Quant. Grav.* **27**, 215017 (2010) [arXiv:1101.3569 [gr-qc]].
- [40] R. Wald, “Gedanken experiments to destroy a black hole,” *Annals Phys.* **82**, no.2, 548-556 (1974)
- [41] A. Saa and R. Santarelli, “Destroying a near-extremal Kerr-Newman black hole,” *Phys. Rev. D* **84** (2011), 027501 [arXiv:1105.3950 [gr-qc]].
- [42] H. M. Siahhaan, “Destroying Kerr-Sen black holes,” *Phys. Rev. D* **93**, no.6, 064028 (2016) [arXiv:1512.01654 [gr-qc]].
- [43] H. M. Siahhaan and P. C. Tjiang, “Destroying Kaluza-Klein and Kerr-Newman black holes,” [arXiv:2108.06523 [gr-qc]].
- [44] L. Rezzolla and O. Zanotti, “Relativistic Hydrodynamics,” Oxford University Press, 2013, ISBN 978-0-19-174650-5, 978-0-19-852890-6
- [45] F. Bacchini, B. Ripperda, A. Y. Chen and L. Sironi, “Generalized, energy-conserving numerical simulations of particles in general relativity. I. Time-like and null geodesics,” *Astrophys. J. Suppl.* **237**, no.1, 6 (2018) [arXiv:1801.02378 [astro-ph.HE]].
- [46] E.ourgoulhon, “3+1 Formalism in General Relativity,” Springer, 2012,
- [47] R. Gold, A. E. Broderick, Z. Younsi, C. M. Fromm, C. F. Gammie, M. Mościbrodzka, H. Y. Pu, T. Bronzwaer, J. Davelaar and J. Dexter, *et al.* “Verification of Radiative Transfer Schemes for the EHT,” *Astrophys. J.* **897**, no.2, 148 (2020)
- [48] S. E. Gralla, A. Lupsasca and D. P. Marrone, “The shape of the black hole photon ring: A precise test of strong-field general relativity,” *Phys. Rev. D* **102**, no.12, 124004 (2020) [arXiv:2008.03879 [gr-qc]].
- [49] Y. Meng, X. M. Kuang, X. J. Wang, B. Wang and J. P. Wu, “Images from disk and spherical accretions of hairy Schwarzschild black holes,” *Phys. Rev. D* **108**, no.6, 064013 (2023) [arXiv:2306.10459 [gr-qc]].
- [50] W. Zeng, Y. Ling, Q. Q. Jiang and G. P. Li, “Accretion disk for regular black holes with sub-Planckian curvature,” *Phys. Rev. D* **108**, no.10, 104072 (2023) [arXiv:2308.00976 [gr-qc]].
- [51] S. Guo, G. R. Li and E. W. Liang, “Optical appearance of a thin-shell wormhole with a Hayward profile,” *Eur. Phys. J. C* **83**, no.7, 663 (2023) [arXiv:2210.03010 [gr-qc]].
- [52] F. H. Vincent, S. E. Gralla, A. Lupsasca and M. Wielgus, “Images and photon ring signatures of thick disks around black holes,” *Astron. Astrophys.* **667**, A170 (2022) [arXiv:2206.12066 [astro-ph.HE]].
- [53] J. L. Rosa, “Observational properties of relativistic fluid spheres with thin accretion disks,” *Phys. Rev. D* **107**, no.8, 084048 (2023) [arXiv:2302.11915 [gr-qc]].
- [54] J. L. Rosa, C. F. B. Macedo and D. Rubiera-Garcia, “Imaging compact boson stars with hot spots and thin accretion disks,” *Phys. Rev. D* **108**, no.4, 044021 (2023) [arXiv:2303.17296 [gr-qc]].
- [55] J. L. Rosa, D. S. J. Cordeiro, C. F. B. Macedo and F. S. N. Lobo, “Observational imprints of gravastars from accretion disks and hot spots,” *Phys. Rev. D* **109**, no.8, 084002 (2024) [arXiv:2401.07766 [gr-qc]].
- [56] C. F. B. Macedo, J. L. Rosa and D. Rubiera-Garcia, “Optical appearance of black holes surrounded by a dark matter halo,” *JCAP* **07**, 046 (2024) [arXiv:2402.13047 [gr-qc]].
- [57] L. F. D. da Silva, F. S. N. Lobo, G. J. Olmo and D. Rubiera-Garcia, “Photon rings as tests for alternative spherically symmetric geometries with thin accretion disks,” *Phys. Rev. D* **108**, no.8, 084055 (2023) [arXiv:2307.06778 [gr-qc]].
- [58] M. F. Fauzi, H. S. Ramadhan and A. Sulaksono, “Anisotropic gravastar as horizonless regular black hole spacetime and its images illuminated by thin accretion disk,” *Eur. Phys. J. C* **84**, no.11, 1145 (2024) [arXiv:2411.12358 [gr-qc]].
- [59] F. D. Ryan, “Gravitational waves from the inspiral of a compact object into a massive, axisymmetric body with arbitrary multipole moments,” *Phys. Rev. D* **52**, 5707 (1995)

- [60] F. Ozel, D. Psaltis and Z. Younsi, “Black Hole Images as Tests of General Relativity: Effects of Plasma Physics,” *Astrophys. J.* **941**, 88 (2022) [arXiv:2111.01123 [astro-ph.HE]].
- [61] V. C. J. M., A. V. J. A., F. D. Lora-Clavijo, O. M. Pimentel and O. V. J. E, “OSIRIS: a new code for ray tracing around compact objects,” *Eur. Phys. J. C* **82**, 103 (2022) [arXiv:2202.00086 [gr-qc]].
- [62] D. Rumler, “Circular geodesic orbits in the equatorial plane of a charged rotating disc of dust,” *Phys. Rev. D* **110**, no.6, 064004 (2024) [arXiv:2405.01998 [gr-qc]].
- [63] C. Y. Chen and Y. Yokokura, “Imaging a semiclassical horizonless compact object with strong redshift,” *Phys. Rev. D* **109**, no.10, 104058 (2024) [arXiv:2403.09388 [gr-qc]].
- [64] A. King, “How Big Can a Black Hole Grow?,” *Mon. Not. Roy. Astron. Soc.* **456**, no.1, L109–L112 (2015) [arXiv:1511.08502 [astro-ph.GA]].
- [65] V. Cardoso and L. Queimada, “Cosmic Censorship and parametrized spinning black-hole geometries,” *Gen. Rel. Grav.* **47**, no.12, 150 (2015) [arXiv:1511.00690 [gr-qc]].
- [66] J. Jiang and Y. Gao, “Investigating the gedanken experiment to destroy the event horizon of a regular black hole,” *Phys. Rev. D* **101**, no.8, 084005 (2020) [arXiv:2003.07501 [hep-th]].
- [67] S. J. Yang, Y. P. Zhang, S. W. Wei and Y. X. Liu, “Destroying the event horizon of a nonsingular rotating quantum-corrected black hole,” *JHEP* **04**, 066 (2022) [arXiv:2201.03381 [gr-qc]].